Proceedings World Geothermal Congress 2026
Calgary, Canada, June 8 – 11, 2026

Investigation of Biochemical Clogging Phenomena Along the Geothermal Doublet Loop

Sabooniha E[1]*, Kermani H[1], Barzegar S[1], Nick H[1]
DTU Offshore, Technical University of Denmark, Copenhagen, Denmark [1]
* E-mail: ehssa@dtu.dk

Keywords: Reactive transport, Scale formation, Biomineralization, Microbial activity, Sulphate reducing bacteria

ABSTRACT

Biogeochemical clogging poses a major challenge to the long-term performance of geothermal systems. This study investigates the coupled effects of microbial activity and mineral formation along a geothermal doublet loop, based on the water composition and operational parameters of a case study well in the West Netherlands Basin. A three-dimensional thermo-hydro-bio-chemical (THbC) reactive transport model is employed to simulate the solute and heat transport during cold-water injection, assuming acetate-rich water that stimulates sulfate-reducing bacteria (SRB) activity. The model dynamically captures the feedback between biotic and abiotic precipitation, biofilm accumulation, and the resulting porosity and permeability alteration throughout the reservoir. In addition, wellbores and surface facilities are included to evaluate thermodynamic shifts in temperature and pressure along the surface and wellbore streams. Results demonstrate how biomineralization can locally alter concentration plume distribution, underscoring the importance of microbial control strategies for maintaining geothermal system performance.

1 INTRODUCTION

The extraction and circulation of geothermal fluids disturb the natural equilibrium of subsurface systems. When deep formation fluids are brought to the surface, they experience rapid cooling and depressurization, often becoming oversaturated with respect to various mineral phases (Bonte et al (2013), Fournier (1977)). These changes promote mineral precipitation, causing scale deposition within wells, pipelines, and surface equipment such as heat exchangers and degassers. In addition, the continuous temperature and pressure fluctuations during production and reinjection cycles can trigger complex fluid–rock and fluid–microbe interactions inside reservoir, leading to biofilm development, mineral precipitation, and reservoir souring (Lerm et al (2013), Sharp et al (2014), Sabooniha & Nick (2024), Mahmoodi & Nick (2024)). Collectively, these coupled processes reduce permeability, impair injectivity (e.g. Mahmoodi & Nick (2022)), and shorten the operational lifespan of geothermal systems.

Previous studies have extensively examined the mechanisms and mitigation strategies associated with clogging in geothermal environments. Wei Song et al (2020) classified clogging into three main categories of physical, chemical, and biological, and emphasized the need for real-time monitoring and risk-intelligent management to ensure stable reinjection performance. Kamila et al (2021) further highlighted the importance of site-specific assessment of geothermal water chemistry prior to reinjection and reviewed operational strategies such as cooling ponds, brine dilution, and chemical inhibition for reducing scaling tendencies.

The impact of thermodynamic and redox shifts on clogging has also been studied. Changes in CO_2 partial pressure and redox state during cold-water injection can drive mineral precipitation and permeability loss (Su et al., 2018). Laboratory and field studies across Europe have confirmed that carbonate and sulfate scaling often coincide with microbial processes (Birner et al (2015), Markó et al (2021), Wanner et al (2017)). Sulfate-reducing bacteria (SRB) are of particular concern due to their ability to produce hydrogen sulfide under anaerobic conditions, leading to corrosion, metal sulfide scaling, and biofilm accumulation. These biomineralization pathways accelerate permeability impairment and can propagate from the reservoir to the surface loop. Modeling tools can successfully reproduce sulfate and carbonate scaling behavior under varying thermal and geochemical conditions, reinforcing the need to include biologically driven reactions in reactive transport simulations (García et al (2005)).

The present study focuses on biogeochemical clogging mechanisms and their impact on system performance under representative geothermal operating conditions. Using representative water chemistry and mineralogical characteristics from a geothermal field in the West Netherlands Basin as model input, the work examines the

evolution of porosity, permeability, during cold-water reinjection enriched with total organic compound (TOC), which stimulates SRB growth. The results shed light on how microbial activity and mineralization jointly shape flow and transport behavior within geothermal doublet systems.

2 METHODOLOGY

This study employs a thermo-hydro-bio-chemical (THbC) modeling framework to quantify the impact of microbial activity and biogeochemical precipitation on flow, heat transport, and injectivity in a geothermal doublet loop. The workflow couples 1D reactive transport in surface pipelines and wellbores with zero-dimensional surface facility nodes representing the degasser, heat exchanger, and pumps. These domains are dynamically linked to a 3D reservoir model, with sequential exchange of updated flow and chemistry at each time step. Reactive transport in the pipelines is coupled with pipe hydraulics, while the reservoir is solved as a 3D Darcy–advection–diffusion–reaction system incorporating porosity–permeability feedback (Figure 1). A finite element solver computes flow and transport in both domains, and PHREEQC is employed as the geochemical reaction solver.

The 3D model includes a 100 m-thick reservoir bounded by 450 m overburden and underburden layers. The domain spans 3 km, with wells placed 750 m from the boundaries. A geothermal gradient of 30 °C/km is applied. The No-flow boundaries are imposed on the top, bottom, and interlayer interfaces (except for conductive heat transfer), and lateral boundaries are open. The injection well maintains a constant inlet temperature, the production well uses an outflow condition, and the initial reservoir pressure is 230 bar.

In the next sections, details of governing equations for flow, heat, solute transport, and microbial kinetics, together with the numerical sequencing are elaborated. The framework will then be applied to a scenario in which total organic carbon (TOC), modeled as acetate, is sufficient to stimulate sulfate-reducing bacterial activity.

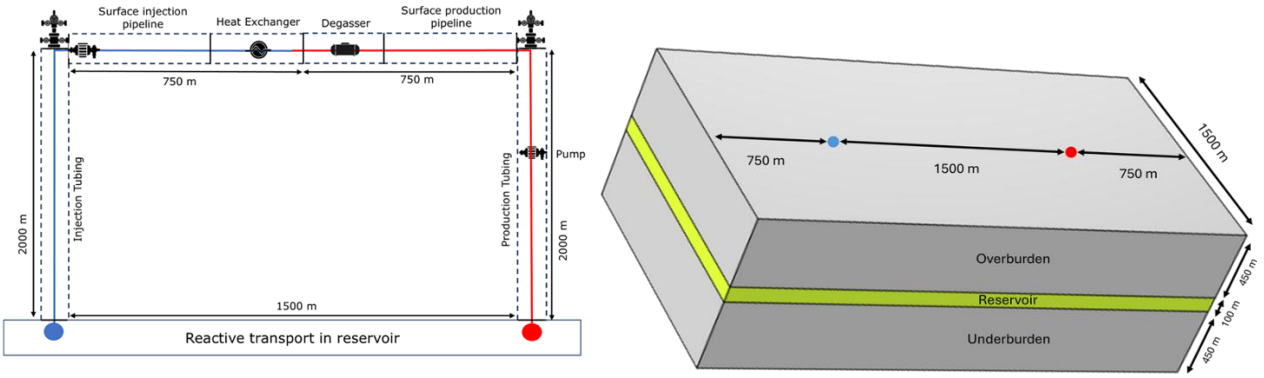


Figure 1. Schematic of coupled model used for assessing biochemical scale in geothermal loop systems

2.1 Reactive flow in tubing, pipelines, and surface facilities

Surface flow from the production wellhead to the degasser, through the heat exchanger, and back to the injection wellhead is modeled with a 1D PHREEQC transport block coupled to a 1D pipe-flow model. This coupling captures frictional pressure losses, composition changes from mineral reactions, and (scale-induced diameter reduction.

The transport model in the wellbore and surface stream is governed by the advection-diffusion equation:

$$\frac{dc}{dt} = -v\frac{dc}{dL} + D\frac{d^2c}{dL^2} - \frac{dq}{dt} \quad (1)$$

In the above equation, v*(m/s)* is the water velocity in pipeline, *L(m)* is the pipe or tubing length, and *D* (m^2/s) is the diffusion coefficient of the solute in water. Moreover, *q(M)* is the solute concentration in the precipitated phase. To account for the hydraulic pressure drop across the pipe section, Darcy–Weisbach equation is used for each cell as follows:

$$\Delta p = f_d \frac{L\rho_w v^2}{2D_p} \quad (2)$$

$$f = \begin{cases} \dfrac{64}{Re}, & if\ Re < 2000\ (Laminar) \\ Solution\ of\ \dfrac{1}{\sqrt{f}} = -2lo\,g\left(\dfrac{\in/_D}{3.7} + \dfrac{2.51}{Re\sqrt{f}}\right) = 0, & if\ Re > 2000\ (Turnulent) \end{cases}$$

Where f_d is darcy friction coefficient, ∈ (m) is the pipe roughness. To determine the Darcy friction factor under turbulent flow conditions, an iterative numerical approach is utilized. The following equations are applied for production and injection pump pressures:

$$P_{Production\ pump} = \Delta H_{f_p} + P_{degasser} + P_{H_p} \quad (3)$$

$$P_{Injection\ pump} = \Delta H_{f_i} + P_{inlet} - P_{H_i} - P_{wh} \quad (4)$$

Where ΔH_{f_p} represents the frictional pressure loss in the production pipeline from the pump location to the degasser, ΔH_{f_i} denotes the frictional pressure loss from the injection wellhead to the injection point within the reservoir, P_{H_p} is the hydrostatic pressure of the water column above the production pump, while P_{H_i} refers to the hydrostatic pressure within the injection well. P_{inlet} refers to the hydrostatic pressure within the injection well, and P_{wh} is the pressure of the water at injection well head.

The production and injection tubing are modeled with a fixed diameter of 14 cm for simplicity. Brine is injected and produced at a steady rate of 200 m^3/h. During production, dissolved gases are released in a degasser, while the fluid remains undersaturated with respect to gases throughout the wellbore prior to reaching the degasser. In the model, inert nitrogen gas is used at a constant pressure in the degasser to account for the gas liberation from the brine. It is assumed that the production filters effectively remove particles larger than 1 μm, so fine migration and particle-related issues are excluded from the model. The brine is then cooled to 35°C at the heat exchanger and subsequently pressurized back to maintain the 200 m^3/h injection rate into the reservoir. Notably, no chemicals are added to the water at the surface before the injection phase.

Reactive flow in wellbores and pipelines is simulated by discretizing the stream into computational cells. The surface time step (Δt_s) corresponds to the fluid travel time across each cell, satisfying the Courant–Friedrichs–Lewy (CFL) condition for stability. While this time step is explicitly controlled, PHREEQC internally refines substeps through its implicit solver to ensure accurate reaction calculations. The pressure used for reactions is approximated as the mean of inlet and outlet values for each cell.

2.2 Reactive flow and heat transfer in the reservoir

Fluid flow through the reservoir is described by Darcy's law:

$$\frac{Q}{A} = -\frac{K}{\mu_w}\nabla p \quad (5)$$

where Q $(^{m^3}/_S)$ is volumetric flow rate, A (m^2) is the cross-section area, K (m^2) is permeability, μ_w $(Pa.s)$ is water viscosity, ∇p (Pa) is a pressure gradient. Advection-diffusion equation is used to solve solute transport:

$$\partial C/\partial t = -u\,.\nabla C + D\nabla^2 C \quad (6)$$

In the above equation, C $(^{mol}/_L)$ is the solute concentration, and u $(^m/_S)$ is the interstitial velocity vector of fluid in the porous media. Additionally, D $(^{m^2}/_S)$ is the molecular diffusion coefficient. For heat transfer, the solute transport equation is applied, with adjustments to thermal velocity based on the thermal retardation factor, and thermal conduction accounted for using the thermal diffusion factor:

For heat transfer, the solute transport equation is applied, with adjustments to thermal velocity based on the thermal retardation factor, and thermal conduction accounted for using the thermal diffusion factor:

$$\frac{\partial T}{\partial t} = -Ru.\nabla T + D_{eff}\nabla^2 T \quad (7)$$

Where R represents the dimensionless thermal retardation factor and D_{eff} $(^{m^2}/_S)$ denotes effective thermal diffusion. The retardation factor and effective thermal diffusion calculation in 3D model is calculated using the following equations:

$$R = \frac{\rho_f C_{p,f}}{(\rho C_p)_{eff}} \quad (8)$$

$$D_{eff} = \frac{\emptyset k_f + \theta_s k_s + \theta_{imf} k_{imf}}{(\rho C_p)_{eff}} \quad (9)$$

$$(\rho C_p)_{eff} = \emptyset \rho_f C_{p,f} + \theta_s \rho_s C_{p,s} + \theta_{imf} \rho_{imf} C_{p,imf} \quad (10)$$

In the above equations, $C_{p,f}$, $C_{p,s}$, $C_{p,imf}$ ($^{J}/_{K.kg}$) represent the specific heat capacities of the moving fluid, solid, and immobile fluid, respectively. Immobile fluid exists only in the overburden layer, where the properties of overburden water are similar to those of reservoir water. Likewise, k_f, k_s, k_{imf} ($^{W}/_{m.K}$) depicts thermal conductivity of each component. The parameters $\emptyset$ and θ indicate porosity and solid volume fraction in the model.

In the modeling, at each time step, fluid velocity is calculated, followed by sequentially solving the heat and transport equations. Reaction calculations are then performed, producing updated water and solid compositions for each cell. After each timestep, the permeability and porosity in the system is updated and a new pressure gradient and velocity is derived in the reservoir. The porosity and permeability reduction is calculated using the following equation:

$$\emptyset = \emptyset_i - \frac{\sum_{t=1}^{n}(V_p d_s + V_p m_{bf})}{V_b} \quad (11)$$

$$K = \frac{{d_p}^2 \emptyset^3}{180(1-\emptyset)^2} \quad (12)$$

Where $\emptyset_i$ is the initial porosity, d_s is the volume of total precipitated solid per one litre of water, m_{bf} is the total biofilm volume per one litre of water. V_p, V_b represent pore volume and bulk volume of interest zone respectively. grain size diameter (d_p) Here for the simplification, the permeability of biofilm is assumed to be zero. Grain size diameter (d_p) is assumed 0.00014 (m) for all minerals. It is computed and adjusted using the initial porosity and permeability values through the Carman-Kozeny (CK) relationship.

2.3 Microbial and Mineral Reaction Kinetics

2.3.1 Mineral reactions

The models assume an initial equilibrium by equilibrating the surface-extracted water with the reservoir rock composition (Table 2), representing the in-reservoir water chemistry prior to production (Table 1). The phreeqc.dat database was selected for reaction calculations due to acceptable prediction accuracy and inclusion of redox reactions, essential for microbial activity calculations.

In the current study, and in line with recommendations from previous research in the literature (60,61), kinetic reactions have been implemented to model the precipitation and dissolution of the most likely minerals (Calcite, Barite, Pyrite, Quartz), while less likely minerals (Fluorite and Talc) have been treated as instantaneous to reduce computational cost (Table 3). The kinetic reactions parameters, including specific surface areas, are extracted from (Zu et al (2016), Zhang et al, (2019), Gaus et al (2005), Gao et al (2018), Michot et al (71)). Mineral reactions typically occur at specific surface sites, making reactive surface areas much smaller than geometric ones. In this regard, a scaling factor of 0.001 is applied to all minerals to account for this difference.

2.3.2 Microbial reactions

In geothermal doublet systems, most laboratory studies have examined scale formation caused by chemical disequilibrium and biomineralization triggered by microbial activity during cold-water injection. However, the combined influence of biofilm growth and mineral precipitation is also very important.

This study proposes a simulation framework to evaluate the interplay between reservoir mineralogy, biochemical reaction kinetics, and the influence of microbial activity on biochemical clogging. To this end, in addition to modeling the kinetics of various minerals, the kinetics of sulfate-reducing bacteria including growth, decay, attachment, and detachment are explicitly incorporated to capture their role in the system. To simulate SRB microbial activity a Dual-Monod model is implemented, linking bacterial growth rates to the availability of both electron acceptors and donors:

$$\mu = \mu_{max} Y \frac{C_A}{C_A + K_A} \frac{C_D}{C_D + K_D} \quad (12)$$

Where $\mu(mol/sec)$ and $X(mol)$ are growth rate and current moles of bacteria cells respectively. In the rate coefficient equation, $\mu_{max}(1/s)$, $C(mol/kgw)$ and $K(mol/kgw)$ represent the maximum specific growth rate, concentration, and half saturation constant, respectively. The indices A and *D* represent the electron acceptor (sulfate) and electron donor (acetate), respectively. The yield coefficient *Y (mol X/mol of substrate)* is defined as the ratio of microbial production rate to substrate consumption rate. The maximum specific growth rate is temperature dependent. To capture this relationship, the following expression is applied (Rosso et al (1995)):

$$\mu_{max} = \begin{cases} if\ T < T_{min} : 0 \\ if\ T_{min} < T < T_{max} : \mu_{opt}\eta(T) \\ if\ T > T_{max} : 0 \end{cases} \quad (13)$$

Here, T (°C) is the temperature at which the maximum specific growth rate is being evaluated. T_{min} (°C) and T_{max} (°C) represent the lower and upper temperature limits for microbial activity. μ_{opt} denotes the highest possible maximum specific growth rate, occurring at the optimum temperature**,** where the temperature multiplier $\eta(T) = 1$. The temperature multiplier $\eta(T)$ is calculated using the following expression:

$$\eta(T) = \frac{(T-T_{max})(T-T_{max})^2}{(T_{opt}-T_{min})[(T_{opt}-T_{min})-(T-T_{opt})(T_{opt}-T_{max})(T_{opt}+T_{min}-2T)]} \quad (14)$$

This study assumes a unified set of parameters to represent the entire bacterial community of each type (Table 1) (Vashereh et al (2021)). Additionally, the microbial decay coefficient is set to 2% of growth rate.

Table 1. Summary of microbial growth kinetic parameters

$\mu_{max}(1/h)$	$T_{max}(°C)$	$T_{min}(°C)$	$T_{opt}(°C)$	$K_d(M)$	$K_a(M)$	$c_{initial}(M)$	$Y(\frac{mol_x}{mol_s})$
0.191	47	16	37	0.00275	0.00275	0.0000439	0.032

In flowing systems, biofilm growth is governed by the balance between microbial proliferation, shear-induced detachment, and attachment of planktonic cells. Here, biofilm refers to immobile biomass and biomass to mobile cells, with growth confined to a thin nutrient-rich active layer. The characteristic thickness (δ) of this metabolically active zone is controlled by the balance between substrate diffusion and consumption, described by Pirt (1967):

$$\delta = \sqrt{2C_0 D_s Y_{im}/\mu_{im}^{\cdot}} \quad (15)$$

where C_0 (*mol/kgw*) is the substrate concentration, $D_s(m^2/s)$ is the substrate diffusion coefficient, Y_{im} (*kg of X/mol of substrate*) is the yield coefficient for biofilm, and $\mu_{im}^{\cdot}(1/sec)$ depicts the biofilm growth rate coefficient. The rate of biofilm growth μ_{im} (*mol/sec*) is then expressed as:

$$\mu_{im} = min\left(\frac{10^6 SA_{rock}\mu_{im}^{\cdot}\rho_{im}\delta}{MW_{im}}\ ,\mu_{im}^{\cdot}X_{im}\right) \quad (16)$$

In the above equation $SA_{rock}(m^2/kgw)$, ρ_{im} (g/cm^3), $MW_{im}(g/mol)$, and $X_{im}(g/cm^3)$ represent reactive rock surface area biofilm density, biofilm molar mass, and current biofilm moles in the system respectively. It is assumed that the reactive surfaces of all existing minerals are available for biofilm formation. The concentration and mass of the biofilm are used to estimate X, assuming a representative molar mass of 114(*g/mol*) based on the empirical formula $C_5H_7O_2N$, which characterizes microbial biomass in both biofilm and planktonic forms.

In the current study, two of the most widely used formulations, which have been independently validated for biofilm development in porous media, are selected for accounting detachment and attachment rate in in the kinetic rate calculation of biofilm and biomass (Brovelli et al., 2009; Coyte et al., 2017).

$$K_{att} = \frac{3(1-\emptyset)u_p\eta}{2d_p} \quad (17)$$

$$K_{det} = C_d\left[\frac{\tau_w u_p(1-\emptyset)^2}{d_p\emptyset^3}\right]^{0.58} \quad (18)$$

In the above equations, $K_{att}(1/s)$, $K_{det}(1/s)$, $u_p(m/s)$ depicts the attachment rate, detachment rate, and pore velocity. $d_g(m)$ is the grain size diameter, and η is the collector efficiency. In this study we have chosen the average value of 2×10^{-3} as the coefficient used for simulations according to Bozorg et al (2015). Rittmann et al (2001) proposed a widely used value of 2.29×10^{-6} for C_d, which has been adopted in numerous studies.

2.4 Reservoir properties, mineralogy, and water composition

The modeled field case represents a low-enthalpy geothermal project in the West Netherlands Basin, selected for its well-documented water chemistry and operational data. Hot water at 60 °C is produced from a depth of 2000 m at a bottomhole pressure of 230 bar. The representative water composition (Table 2) was determined using ICP-MS and ion chromatography. To account for microbial activity, 1 mmol kg^{-1} of acetate is assumed as the organic carbon source, sufficient to sustain maximum SRB activity. The reservoir rock is assumed to consist mainly of quartz (90%), with calcite (8%) and pyrite (0.25%) as cementing phases, and minor barite (0.5%), fluorite (0.25%), and talc (1%) included based on geochemical indicators. Porosity and permeability are set to 15% and 500 mD, respectively, for a 100 m-thick reservoir. Thermal properties are adopted from Robertson et al.

Table 2. Water composition used in geochemical modeling

Ionic composition of produced water	Concentration before reservoir equilibrium(ppm)	Concentration after reservoir equilibrium(ppm)
Cl^-	85000	98692
Br^-	536	622
$SO_4{}^{2-}$	220	192.1
$HCO_3{}^-$	190	97.6
F^-	181	4.75
Ba^{2+}	8	4.12
Ca^{2+}	6100	6731
Cu^{2+}	35	0.13
Fe^{2+}	67	60.3
K^+	275	319.1
Mg^{2+}	1000	1210.2
Mn^{2+}	1.3	1.1
Na^+	45000	53842
Pb^{2+}	0.06	0.06
Si	20	3.65
Sr^{2+}	400	464.4
Zn^{2+}	0.2	0.2
TOC	59	59

3 RESULT AND DISCUSSION

3.1 Wellbores and surface stream pressure and scale analysis

Over the 10-year injection period, the pressures at both the injection and production pumps were tracked to maintain a constant flow rate. As shown in Figure 2, the injection pump pressure increased by about 6 bar when considering near-wellbore reactions. Since the injection pipeline diameter remained nearly constant, this rise is attributed to clogging and changes in fluid viscosity in the near-wellbore region, which together increase flow resistance. A no-reaction case was also analyzed to separately demonstrate the impact of viscosity changes due to cold-water injection. The comparison shows that at the early stage of injection, viscosity effects dominate because scale formation is minimal. However, with continued injection and progressive scale formation, clogging becomes the dominant mechanism controlling the pressure increase at later stages. The production

pump pressure rose by approximately 3 bar over the same period, mainly due to gradual diameter reduction from scaling along the production pipeline, as geochemical and microbial activity near the production well was minimal. These trends highlight how clogging within both the reservoir and surface infrastructure progressively increases pumping demand.

As depicted in Figure 2, after 1.5 years of injection, mineral scaling is primarily concentrated in the upper part of the production tubing close to the pump location. This region experiences the lowest wellbore pressure, which leads to a more pronounced reduction in the internal tubing diameter. As the system evolves, the scale accumulation zone progressively shifts toward the bottomhole section of the well, driven by changes in nucleation site availability and the associated kinetic conditions governing precipitation.

As water ascends to the production wellhead, only the carbonate concentration changes notably, while other ions remain relatively stable. Most compositional shifts occur in surface facilities, driven by pressure and temperature drops and gas release. CO_2 degassing sharply reduces carbonate concentration in the degasser, while cooling in the heat exchanger enhances barite precipitation, as its solubility decreases markedly at lower temperatures.

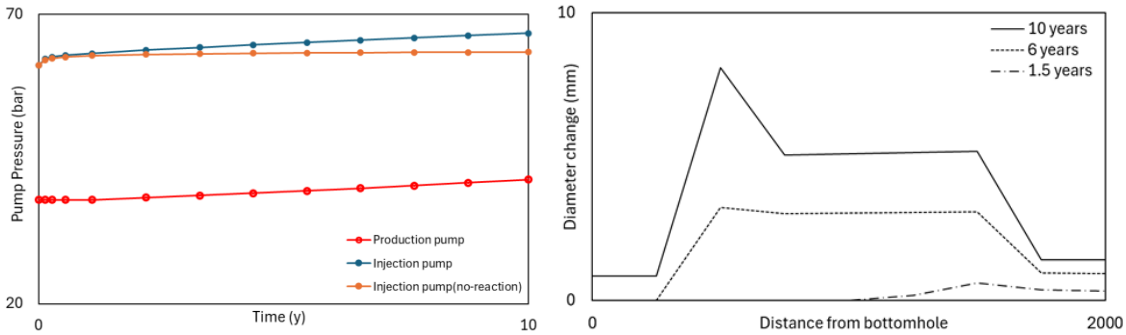


Figure 2. Left: Pressure evolution at the injection and production pumps over 10 years of operation. Right: Diameter change in the production tubing 10 years of operation

3.2 Temperature and pressure profile inside reservoir

Temperature plays a critical role in controlling the onset of microbial activity within geothermal systems. When cold fluid is injected into a hot reservoir, the resulting temperature drop alters microbial equilibria, triggering the growth of in-situ microbes such as sulfate-reducing bacteria (SRB) and the subsequent formation of biofilm, and biominerals such as calcite and pyrite. Figure 3 illustrates the cold front profile after 10 years of injection, mapped on a 2D cross-section on xy and xz planes. This thermal front effectively delineates the boundary between microbiologically inactive and active zones, providing a basis for evaluating the spatial extent of microbial souring and associated geochemical phenomena.

As illustrated in Figure 3, Pressure profile distribution also indicates the pressure increase around the injection wellbore. This is caused by the scaling formed around the injector and propagation of the cold front affecting the hydrodynamic of the flow by altering water viscosity profile in the reservoir.

3.3 Water concentration and scaling profiles inside reservoir

One of the main benefits of 3D simulations is their ability to represent the spatial evolution of heat and solute dispersivity, providing a more realistic picture of reactive transport in geothermal systems. To better visualize these effects, 2D top-view slices were extracted from the 3D model, showing the spatial distribution of key dissolved ions during the injection period (Figure 4).

Over time, the solute front propagated from the injector toward the producer, reaching about the midpoint of the reservoir. Calcium and carbonate concentrations gradually returned toward their initial levels, though carbonate showed local deviations caused by calcite precipitation. This trend reflects an increase in carbonate ions in the injected water, which was initially depleted by CO_2 degassing, driven by microbial activity in the reservoir. Elevated concentrations of carbonate and calcium promote continuous calcite formation, confirming the strong coupling between biogeochemical reactions and transport processes.

Sulfate concentrations declined by nearly half due to sulfate-reducing bacterial (SRB) activity. Concurrently, dissolved iron decreased as sulfide produced by SRB reacted with iron to form iron sulfide. This process underscores the dominant influence of microbial reduction on geochemical transformations near the injector.

The injected water contained only trace amounts of barium, as most barite had already precipitated within the surface facilities prior to reinjection. Consequently, barite precipitation in the reservoir is considered negligible.

The main minerals precipitating around the wellbore were calcite, pyrite, and to a lesser extent, fluorite. Figure 4 also illustrates the changes in the concentration of these minerals within 500 meters around the injector.

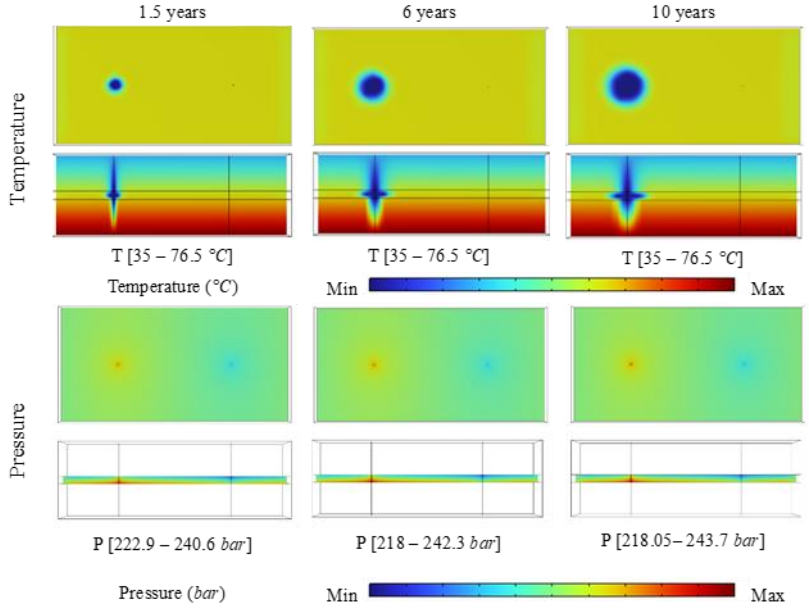


Figure 3. Temperature and pressure distribution after 10 years of injection

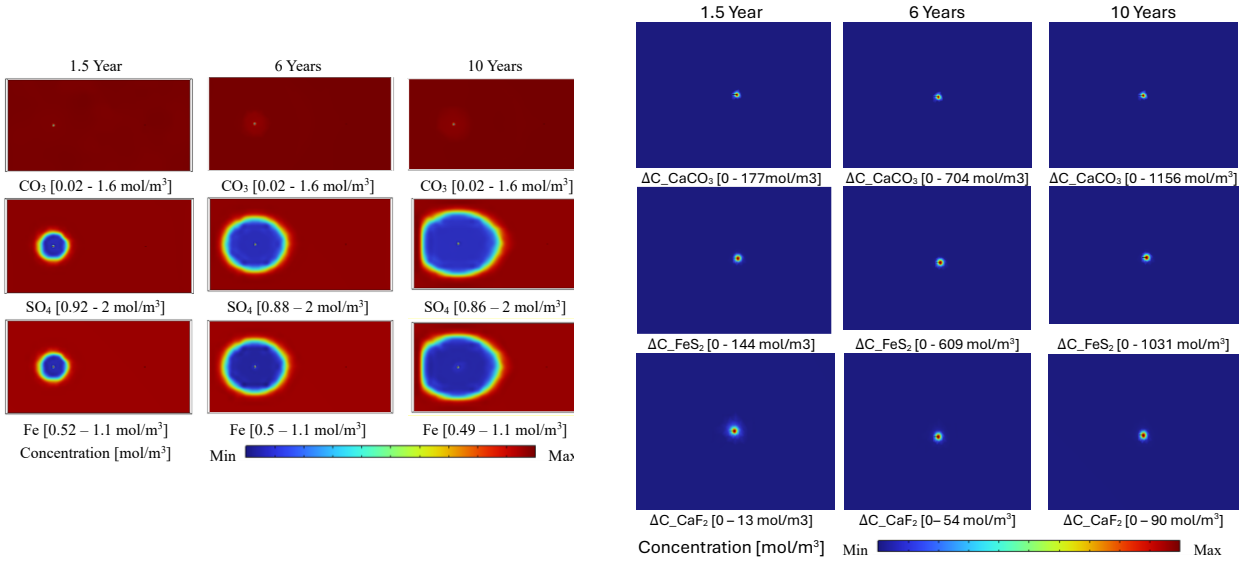


Figure 4. 2D top-view distribution profiles of dissolved ionic species and changes of mineral scales

3.4 Biofilm and biomass profiles

To evaluate microbial activity in terms of the dynamic balance between planktonic biomass and biofilm, a 2D spatial profile of their concentrations in xy and xz plane was mapped from the injector toward the producer. Figure 11.a shows the evolution of biofilm concentration at different time points during the simulation. Biofilm initially develops near the injector, where thermal and nutrient conditions are most favorable. As the simulation progresses, a distinct spatial gradient emerges, with dense biofilm formation close to the well and decreasing concentrations farther away. The corresponding biomass distribution indicates strong detachment near the injector; however, the biomass concentration remains high in the immediate vicinity of the wellbore. This suggests consecutive reattachment to neighboring biofilm layers located just beyond the sharp velocity decline region surrounding the injector.

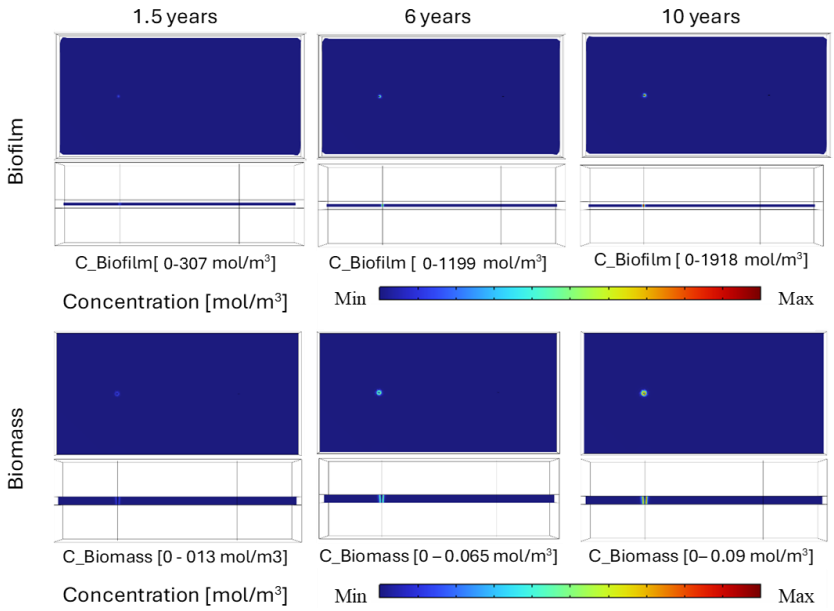


Figure 5.Biofilm and biomass concentration distribution in the reservoir

4 CONCLUSION

This study demonstrates, through a thermo-hydro-bio-chemical (THbC) framework, how microbial activity and biomineralization contribute to clogging and injectivity decline under representative geothermal operating conditions. Using site-representative water chemistry and mineralogy from a geothermal field in the West Netherlands Basin as model input, the model resolves the evolution of porosity and permeability during cold-water reinjection enriched with total organic carbon, which stimulates SRB growth. By explicitly coupling flow, heat transport, microbial growth (including shear-induced detachment and attachment), and geochemistry, the results show that sulfate-reducing bacteria and biofilm development modify local water chemistry and promote calcite and pyrite precipitation near the injection well. Scaling is also captured along the wellbore, pipelines, and surface facilities, and its cumulative impact is reflected in the increasing pressure demand of the injection and production pumps as well as changes in injection water composition. These interacting processes progressively increase flow resistance and injection pressure, as captured by the fully coupled THbC model.

Future studies will focus on validating the model using real geothermal field case studies and can further extend the framework to include geomechanical effects and interactions among multiple microbial strains (e.g., inhibition or competition).

Acknowledgements

This study was supported by the Independent Research Fund Denmark (Project PInClog, grant DFF 2035-00358B).

REFERENCES

Lerm S, Westphal A, Miethling-Graff R, Alawi M, Seibt A, Wolfgramm M, et al. Thermal effects on microbial composition and microbiologically induced corrosion and mineral precipitation affecting operation of a geothermal plant in a deep saline aquifer., *Extremophiles*, **17(2)**, (2013):311–27.

Fournier RO. Chemical geothermometers and mixing models for geothermal systems, **5**, (1977), *Geothermics*, 41–50.

Bonte M, Röling WFM, Zaura E, Van Der Wielen PWJJ, Stuyfzand PJ, Van Breukelen BM. Impacts of shallow geothermal energy production on redox processes and microbial communities. *Environ Sci Technol*, **47(24)**, (2013), 14476–84.

Sharp CE, Brady AL, Sharp GH, Grasby SE, Stott MB, Dunfield PF. Humboldt's spa: microbial diversity is controlled by temperature in geothermal environments., *ISME J*, **8(6)**, (2014), 1166–74.

Sabooniha, E., & Nick, H, Uncertainty Analysis of Chemically Induced Scale Formation in Low to Medium Enthalpy Geothermal Reservoirs, *Proceedings*, 85th EAGE Annual Conference and Exhibition, Oslo, Norway (2024).

Mahmoodi, A., & Nick, H. M. (2024). Microbial Sulfate Reduction in Underground Reservoirs: Learnings from Full-Field Modeling and Field Data. SPE Journal, 29(08), 4376-4394.

Mahmoodi, A., & Nick, H. M. (2022). The interplay between microbial reservoir souring and barite scale formation in hydrocarbon reservoirs. Journal of Cleaner Production, 377, 134234.

Song W, Liu X, Zheng T, Yang J. A review of recharge and clogging in sandstone aquifer, *Geothermics*, **87**, (2020);101857.

Kamila Z, Kaya E, Zarrouk SJ. Reinjection in geothermal fields: An updated worldwide review 2020. Geothermics. **89**, (2021), 375–6505.

Su Y, Yang F, Wang B, Jia Z, Duan Z. Reinjection of cooled water into sandstone geothermal reservoirs in China: a review. *Geosciences Journal*, **22**, (2018), 199–207.

Birner J, Seibt A, Hinrichs 3torsten, Seibt P, Wolfgramm M. Removing and Reducing Scalings – Practical Experience in the Operation of Geothermal Systems. 2015.

Wanner C, Eichinger F, Jahrfeld T, Diamond LW. Causes of abundant calcite scaling in geothermal wells in the Bavarian Molasse Basin, Southern Germany, *Geothermics*, **70**, (2017), 324–38.

Markó A, Mádl-Sz J, Brehme M. Injection related issues of a doublet system in a sandstone aquifer-A generalized concept to understand and avoid problem sources in geothermal systems, *Geothermics*, **97**, (2021), 102234.

García AV, Thomsen K, Stenby EH. Prediction of mineral scale formation in geothermal and oilfield operations using the extended UNIQUAC model Part I. Sulfate scaling minerals. Geothermics, **34, (**2005), 61–97.

Zhen-Wu BY, Dideriksen K, Olsson J, Raahauge PJ, Stipp SLS, Oelkers EH. Experimental determination of barite dissolution and precipitation rates as a function of temperature and aqueous fluid composition. *Geochim Cosmochim Acta*, **194**, (2016), 193–210.

Zhang Y, Hu B, Teng Y, Tu K, Zhu C. A library of BASIC scripts of reaction rates for geochemical modeling using phreeqc. *Comput Geosci*, **133**, (2019),104316.

Gaus I, Azaroual M, Czernichowski-Lauriol I. Reactive transport modelling of the impact of CO2 injection on the clayey cap rock at Sleipner (North Sea), *Chem Geol*, **217**, (2005),319–37.

Gao Z, Xie L, Cui X, Hu Y, Sun W, Zeng H. Probing Anisotropic Surface Properties and Surface Forces of Fluorite Crystals, *Langmuir*, **34(7)**, (2018), 2511–21.

Michot LJ, Villiéras F, François M, Yvon J, Dred RLE, Cases JM. The Structural Microscopic Hydrophilicity of Talc. *Langmuir*,**10(10)**, (1994), 3765–73.

Rosso L, Lobry JR, Bajard S, Flandrois JP. Convenient Model To Describe the Combined Effects of Temperature and pH on Microbial Growth. *Appl Environ Microbiol*, (1995), 610–6.

Veshareh MJ, Nick HM. Growth kinetic and transport of mixed microbial cultures in subsurface environments. *Adv Water Resour*, **153**, (2021),103929.

Pirt SJ. A kinetic study of the mode of growth of surface colonies of bacteria and fungi. *J Gen Microbiol*, **47(2)**, (1967), 181–97.

Bozorg A, Gates ID, Sen A. Impact of biofilm on bacterial transport and deposition in porous media. *J Contam Hydrol*, **183**,109–20.

Rittmann P, McCarty B. *Environmental Biotechnology: Principles and Applications*, *McGraw-Hill Education*, (2001)

Robertson EC. THERMAL PROPERTIES OF ROCKS. *Geological Survey,* Open-File Report 88-441, *(1988)*